The HST-COS Far Ultraviolet Detector: Final Ground Calibration

John Vallerga[a], Jason McPhate[a], Adrian Martin[a], Geoff Gaines[a], Oswald Siegmund[a], Erik Wilkinson[b], Steven Penton[b], and Stephané Béland[b]

[a]Space Science Laboratory
University of California, Berkeley, CA 94720-7450

[b]Center for Astrophysics and Space Astronomy
University of Colorado, Boulder, CO 80309

ABSTRACT

The flight microchannel plate detectors to be used in the Cosmic Origins Spectrograph, a fourth generation instrument for the Hubble Space Telescope, have been calibrated in the laboratory before being integrated into the spectrograph. This paper presents the results of these calibrations that include measurements of the detector quantum efficiency, spatial resolution, spatial linearity, flat field, electronic livetime and the local count rate limit.

Keywords: Microchannel plates, ultraviolet detectors, Hubble Space Telescope, Cosmic Origins Spectrograph

1. INTRODUCTION

The Hubble Space Telescope Cosmic Origins Spectrograph (HST/COS)[1] is an ultraviolet spectroscopic instrument designed to acquire high resolution ($\lambda/\Delta\lambda \sim$ 20-30,000) spectra in the far ultraviolet (90-200nm) and is due to be installed in early 2004.. The optical design relies on large format (200 x 10mm; 32768 x 1024 pixel) microchannel plate (MCP) detectors with delay line anode readouts. The detectors have been developed and built by the Experimental Astrophysics Group at the University of California, Berkeley.

A single COS flight detector has two "segments", each segment a separate windowless MCP detector (MCPs and anode) but sharing a rigid mechanical body mounted in a vacuum assembly. The detector design is based on the Far Ultraviolet Spectroscopic Explorer[2] (FUSE) detectors[3] but with some key modifications to improve its performance. Both the HST/COS and FUSE detectors have two sets (Z-stack) of MCPs that are curved in the spectral dispersion direction to match the focal plane of the spectrograph. Both have an opaque photocathode deposited on the front MCP surface with a fine wire mesh above to increase the QE in the FUV. The main difference between the detectors is the readout anode and electronics. The HST/COS detector employs a cross delay line anode which uses time delay in both x and y axes, which improves the spatial resolution, linearity and readout rate performance. A full description of the detector is in reference 4 and a description of the optimization of the electronics can be found in reference 5.

2. PERFORMANCE SPECIFICATION FOR THE HST/COS DETECTOR

2.1 Statement of Requirements

The performance specifications required for the HST/COS detectors flowed down from the scientific goals of the spectrometer itself. HST/COS was designed to be the most sensitive FUV instrument in its

Correspondence: Email: jvv@ssl.berkeley.edu; Telephone: 510 643 5666

bandpass. Therefore, the emphasis for the detector performance is high QE, low background and high spatial (i.e. spectral) resolution. Other important goals for a Hubble class instrument are stability, dynamic range and wavelength accuracy. With these goals in mind, we developed a Statement of Requirements for the HST/COS Detector that delineated the specific performance specifications the detector had to meet. Table 1 summarizes a subset of these performance specifications for the detector.

Table 1. HST/COS Detector Specifications

Test	Specification
Spatial Linearity (Integral)	Deviation from linear fit of less than ±100μm over 80% of FOV
Spatial Linearity (Differential)	Characterized by uniform flat field of 100 cts. per pixel
Spatial Resolution	< 31μm FWHM in dispersion direction when measured with 25μm slit mask
Maximum Count Rate	40,000 cps per segment, 80,000 cps per detector
Local rate maximum w/o loss of response	5 cts/sec/pore over an area of 1000 μm^2
Livetime	90% at 10,000 cps input, 40% at 100,000 cps input
Quantum Efficiency	1152Å 44% 1216Å 32% 1335Å 25% 1463Å 19% 1560Å 17% 1710Å 11%
Visible Light Response	< 10^{-6} from 4000Å to 6500Å
Dark Count Rate	<0.5 cts. sec^{-1} cm^{-2} (on ground, excluding hotspots)

2.2 Calibration Plan

The detector calibration had to proceed in parallel with its assembly and construction and could not wait until final completion. The main reason for this is the deposition of the CsI photocathode on the top MCP surface. Once it is deposited, exposure to humid air must be minimized to prevent the degradation of this hydroscopic salt and therefore its QE. Also, once deposited, anything that comes in contact with the photocathode can damage it, so the masks used in the linearity and resolution tests can only be used before the photocathode deposition. After QE calibration, the detector is placed in the flight vacuum assembly for its final preconditioning scrub and it should never be removed from a vacuum environment again, unless a major failure occurs. Exposure to air will change the gain stability and possibly affect the QE. Access to the detector is limited to vacuum operations with the door open or in air with the vacuum door closed but illuminated through MgF_2 windows mounted in the door.

The calibration flow can be summarized thereafter:

- Choose MCPs
- Assemble detector (without photocathode or QE enhancement mesh)
- Adjust flight electronics to MCP/anode to optimize imaging performance and fix electronic settings.
- Calibrate spatial linearity and resolution using masks in contact with front MCP surface
- Calibrate local rate performance through two small slits
- Remove masks and calibrate electronic livetime
- Deposit photocathode, install QE grid, and calibrate quantum efficiency

- Install detector in flight vacuum housing with commandable door where it will remain in vacuum forever
- Perform preconditioning "scrub" to stabilize gain for long term operation in space
- Take a deep flat field in the FUV band with a signal to noise ratio of 100
- Finish with standard gain-voltage and background tests which become benchmarks for standard functional tests.

Below we present a subset of the results of these calibrations for the first HST/COS flight detector, designated FUV-01. Sometimes we present data for both Segments A and B to illustrate their differences and similarities. The backup flight detector, FUV-02 has been taken through this calibration as far as the QE calibration, and we include its QE results as well. FUV-01 has been delivered to the University of Colorado, Boulder, where it is undergoing thermal - vacuum testing.

3. CALIBRATION RESULTS

3.1 Spatial Linearity

The photon event position measured by MCP detectors with delay line anodes are derived using analog electronics that are eventually digitized into a pixel array[5]. Though measured time delay is linearly proportional to position on the anode, there are many places in the measurement chain where deviations from a linear position can be imposed. Examples include non-uniform delay line propagation speed, baseline disturbances, cable reflections, non-linear amplifier and ADC response. We measure this non-linearity by placing a electro-formed nickel mask directly on the top surface of the top MCP of the stack and illuminating with UV photons. The two mask patterns we used have uniformly spaced arrays of either small (10 µm diameter) pinholes spaced on 500µm centers or 3 rows of narrow slits (25 x 500µm) spaced 200µm apart with the rows spaced 2.5 mm apart. These masks are used for both measuring the linearity of the detector and the spatial resolution as a function of position. Figure 1 is a partial image (12 x 10 mm) of a slit mask image and a pinhole mask image summed together showing the relative input patterns. Note that the pixel scales are different in the long dispersion direction (X - ~6 µm/pxl) and the cross dispersion direction (Y ~ 25 µm/pxl)

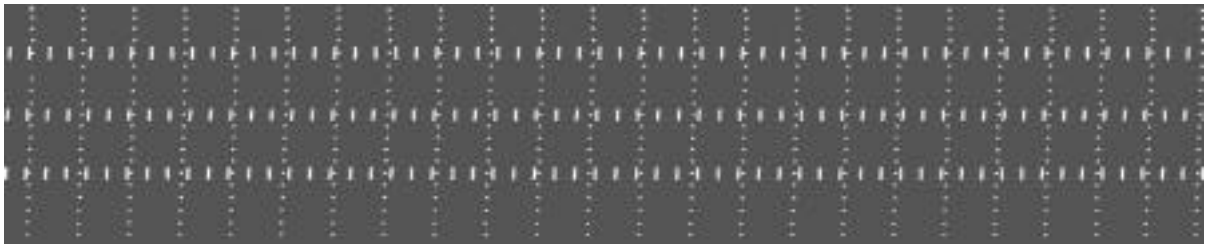

Figure 1. A co-added image of a slit mask and a pinhole mask showing the relative input patterns. For the dimensions see the text.

With the masks in place, we collect a list of photon positions, typically 1000 cts. per slit (pinhole) and derive the centroid and width of each slit, after correcting for any thermal drift during the integration (see reference 6 for details of how we correct for thermal drifts using electronic stimulation of the anode). The residuals in pixels from a linear fit are shown in Figure 2 along with the derived size of each pixel in microns. Over most of the detector, the integral non-linearity (INL), defined as the low frequency deviations from the linear fit, are less than ±10 pxls or 60µm. We believe the dominant cause of this INL are small scale reflections in the anode itself which disrupt the baseline of the fast amplifiers and shift the event timing on the order of tens of picoseconds. However, once measured, this INL can be calibrated out of the data as shown in Figure 3[6].

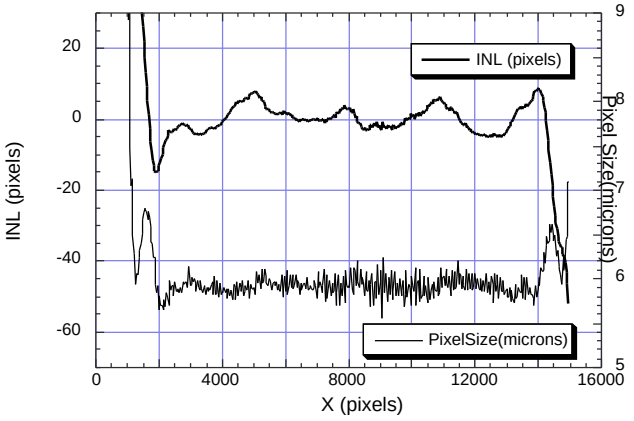

Figure 2. Plot of the integral non-linearity of FUV-01-A as a function of position along the detector in the dispersion direction . Also shown is the derived pixel size in microns

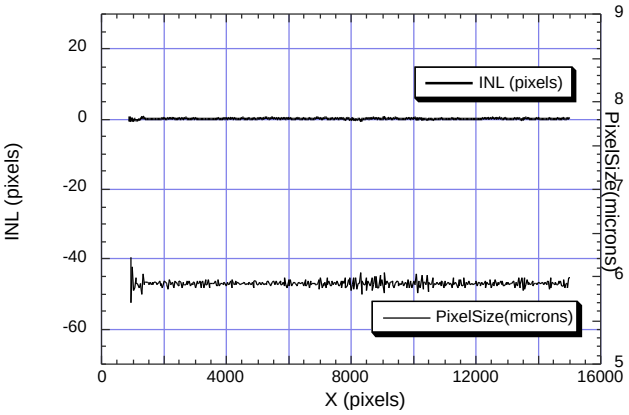

Figure 3. Integral non-linearity after correcting for geometric distortion

3.2 Spatial Resolution

The slit and pinhole mask data also contain information on the width of the individual pinholes and slits. A gaussian function is fit to each and knowing the input fuction, the spatial resolution as a function of position can be derived. Because the pinholes are only 10µm diameter, they better represent the delta function input required to measure the true resolution of the detector. They also give the only information on the spatial resolution in the cross dispersion direction, because the slits are so long in the Y direction. However, the top MCP of the HST/COS detectors have 12µm pores on 15µm centers, so sometimes the pinholes can cover 1, 2 or 3 microchannels, resulting in a greater variance in the measured resolution. The slit width measurements average out this variation by sampling many microchannels but undersample the inherent resolution of the detector. By convolving the slit input function with an assumed gaussian detector response and then fitting with another gaussian, we would expect our 25µm FWHM resolution specification to be equivalent to 31 µm FWHM for the slit data.

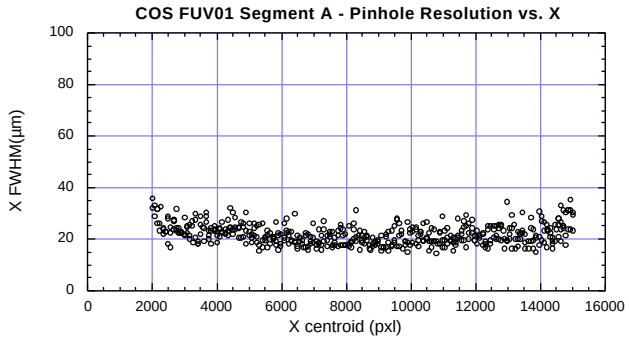

Figure 4. Pinhole resolution in microns FWHM as a function of X position. The specification is 25 µm over 80% of the field of view.

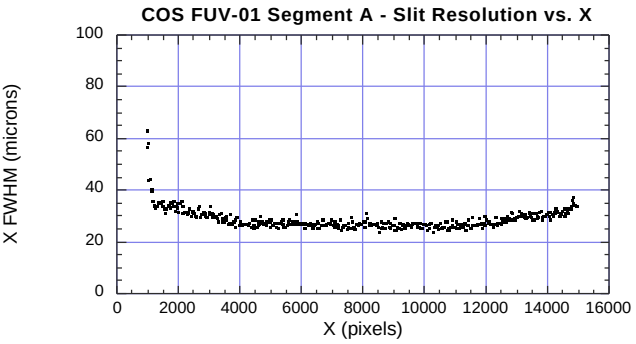

Figure 5. Same as Fig. 4 but using the slit data that averages over more microchannels. The specification is 31 µm over 80% of the field of view.

Figures 4 and 5 show the spatial resolution from the pinhole and slit data for Segments A of FUV-01. segment B is similar. Note that the minimum envelope of the scattered points easily meet the 25µm

FWHM spec. and represent single microchannel inputs. Slit data support this by achieving resolution less than the 31 µm FWHM specification over 80% of the detector area. The Y resolution (not shown) is typically less than 40µm FWHM. Detector resolution can vary as a function of the event position on the delay line due to dispersion and attenuation effects that cause the fast pulses at both ends of the anode to have a smaller amplitude and therefore less signal to noise at the amplifier input [5]. We believe that is what is causing the poorer resolution at the ends, seen more clearly in the slit data.

3.3 Local Rate Test

This test was performed on the FUV-01 detector, Segment A, only, to demonstrate the characteristics of the flight microchannel plates to high, localized fluxes. Since the same batch of MCPs with the same biasing network are used on all flight detector segments, we felt we only had to perform this test on one set of plates. The specification states "The FUV detector shall be capable of supporting maximum local count rates of 5 cts/sec/pore over a circular illuminated region approximately 1000µm^2." For this test, we used a single slit from our standard slit mask used in the resolution and linearity tests. These slits are rectangular holes 25 x 500µm giving a total area of 12,500 µm^2. We believe this larger illumination area is a more conservative test of the MCP as it has been demonstrated many times that larger illuminated regions decrease the local rate capability (per pore) as it decreases the locally stored charge that replenishes the individual pores

To minimize any possible damage to the MCP gain, the individual slit used was away from the center of the segment, at an approximate position of (x,y) = (13900, 530). The UV flux came from a Hg pen ray lamp and the lamp's position and power were controlled to change the count rate. The input rate at the slit ranged from 20 cps to ~5000 cps, so there was minimum deadtime in the electronics.

The gain and pulse height distribution width at the various count rates are shown in Figures 6 and 7. The first sign of a high local flux affecting the MCP output is the widening of the pulse height distribution at ~ 2 cps/pore. As the count rate increases, the pulse height widens, and eventually the average gain begins to decrease above 5 cps/pore (Figure 6). This trend continues and is measured at up to 76 cps/pore (Figure 7, note scale change). At these rates, the pulse height will have degraded enough to affect the response of the detector as events would fall below the lower level discriminators. We believe that the COS MCPs meet the local rate specification, especially given the factor of 12 larger area of illumination in the test setup.

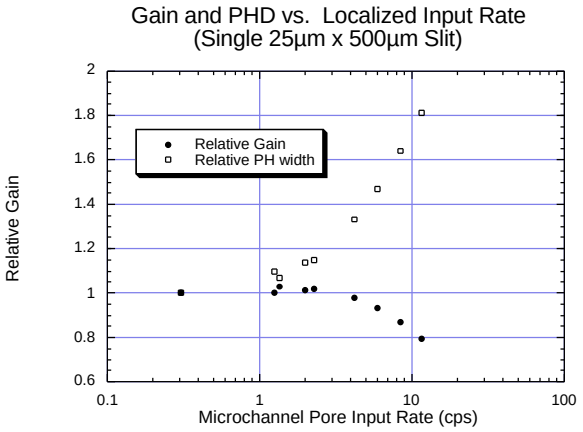

Figure 6. Gain and pulse height width as a function of input count rate per microchannel pore.

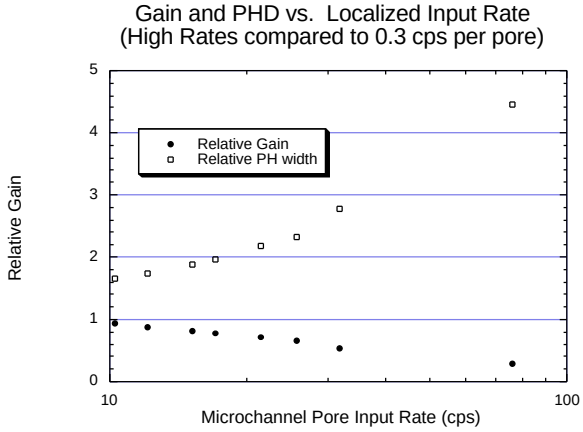

Figure 7. Same as Figure 6 but change of scales to show the higher input rates.

3.4 Detector Livetime vs. Input Count Rate

The HST/COS detector is an imaging photon counter and therefore can lose random events that occur while processing the previous event. The dominant location in the electronics for these collisional losses is in the Time to Digital Converter or TDC, where the time delay is converted into an analog voltage and then converted by an ADC to a digital value. The HST/COS TDC is non-paralyzable[7] in that it locks out incoming events while it processes the previous event. The characteristic time for each event is approximately 7.5 μs as compared to the FUSE TDCs which were ~11μs. This improvement was allowed by changing the anode configuration from the Double Delay Line (DDL) anode used on FUSE to the Helical Cross Delay Line anode used on COS. The DDL anode requires a slower charge sensitive amp for its Y axis determination. Figure 8 shows the output rate of a single TDC (the Digital Event counter or DEC) vs. the input rate from the Fast Event Counter or FEC. The solid line represents input rate = output rate or livetime of 100%. Most HST/COS observations are expected to be much less than 20,000 cps.

The output event streams from both segments of the detector are combined into one data stream via a round robin logic with buffers. Since the events arriving at the round robin are still uncorrelated and random in time, collisions can occur there as well, but the buffering reduces collisional loss significantly. Figure 9 shows this effect where the single stream output rate (Science Data Counter or SDC1) is plotted as a function of the summed rate of DEC-A and DEC-B in the worst case where both DED-A and DEC-B are similar rates.

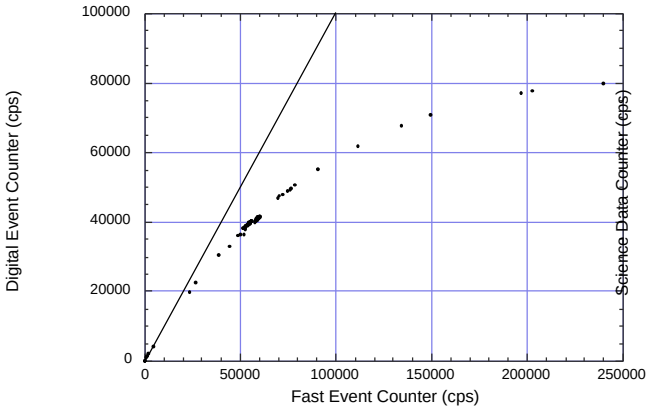

Figure 8. Output vs. input count rate for a single segment of FUV-01. Solid line represents 100% livetime.

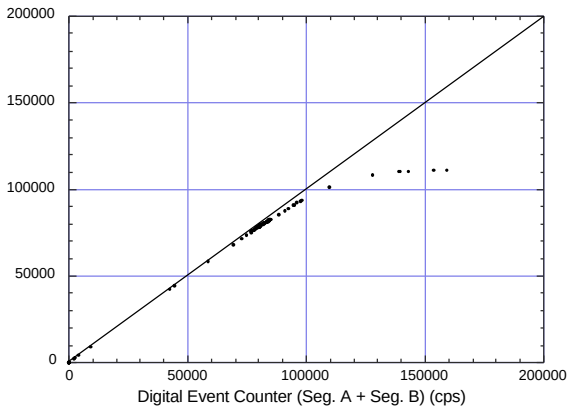

Figure 9. Output count rate of entire detector (both segments) vs. input rate into round robin which combines events from both segments into one data stream

3.5 Quantum Efficiency

Probably the most important specification on the HST/COS detectors is the quantum efficiency, and every effort was made not only to meet the specification, but to exceed it as much as possible. MCPs were screened before the photocathodes were deposited by measuring the QE in the EUV band which has been shown to correlate with a high secondary electron coefficient and therefore a higher probability of detecting the initial photo-electron.

FUV-01 was installed on a 2 axis manipulator in a vacuum calibration chamber at the Space Sciences Laboratory. The manipulator allowed horizontal motion as well as yaw. An FUV (or EUV) beam from a hollow cathode discharge source was sent through a monochromator and then through a pinhole into the tank. This beam could be measured by either an MgF_2 windowed FUV diode biased at 135V or a windowless EUV diode biased at 90V. Each diode's current was monitored by its own electrometer with

a calibrated output response that was 10.0 Volts per picoamp. Errors on the beam measurements were typically 2 millivolts (~200 attoamps).

The MCP count rate was determined from the "Start" pulse from the fast amplifier through a Tennelec Constant Fraction Discriminator (CFD) into a counter. The CFD pulses were shorter than 0.5 µs, so deadtimes at count rates of 10kHz were less than 0.5% and were ignored. A "1%" attenuater mesh was used in all FUV measurements of the MCP count rate so that we could increase the beam intensity to get better signal to noise ratio on the reference diodes. All QE measurements were performed at the center of the detector at an input angle appropriate for the wavelength measured. The beam angle was varied by ±6 degrees in the dispersion direction, re-centering it for each measurement, to check for QE changes as a function of angle.

Initially, we scanned the beam across each segment in the dispersion direction (X) to look for non-uniformities in response. However, for FUV-01, initial results at 1216Å and 1152Å showed very uniform response in X so we did not repeat these integrations at the longer wavelengths We also did not see much change in the angular response when we sampled at every 2 degrees, so we eventually only sampled at –6, 0 and +6 degrees with respect to the initial input angle.

The out of band response was measured using a green and a red Helium/Neon laser and a photodiode. The laser was aimed at the diode outside of the tank and then pointed at both segments to measure a count rate. Great pains were *not* taken to achieve high accuracy, as the measured response was a factor of 7 orders of magnitude below the specification. The QE measured was less than 6 x 10^{-13} for both lasers colors. For FUV-02, we only confirmed that the detector had a similar response to the green laser as FUV-01.

The measured QE's for FUV-01 and FUV-02, Segment A and B are given in Figure 10. They exceed the specifications everywhere measured. Measurement errors (not shown) are typically 1% or less, but do not include the relative or absolute errors of the absolute reference FUV diode calibrated by the National Institute of Standards and Technology (NIST) which are estimated to be 5% (1 standard deviation). The QE numbers are consistent with previous measurements of CsI coated plates of the same type of COS microchannel plates. The variations of response between the plates observed are not uncommon.

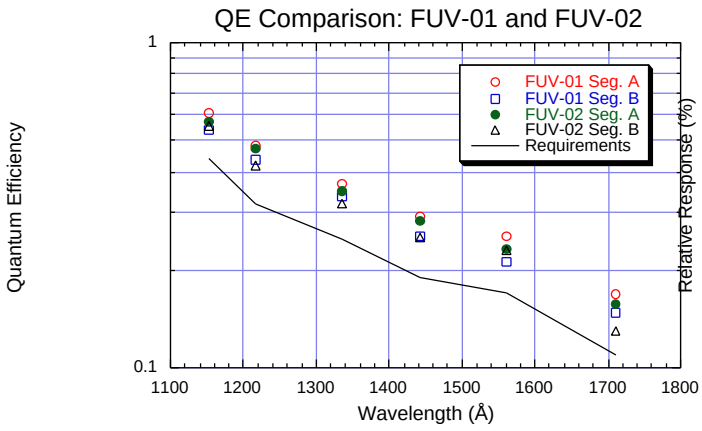

Figure 10. Quantum Efficiency vs. wavelength for FUV-01 and FUV-02, both segments of each. Measurement errors are estimated to be 1% absolute.

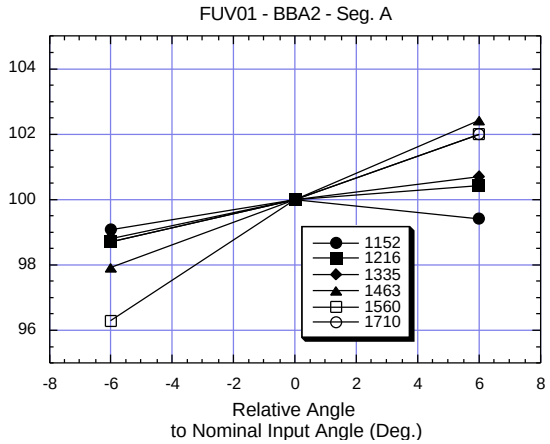

Figure 11. Relative QE vs. relative input angle with respect to the nominal input angle at each wavelength.

At each wavelength, the dependence of the response on relative beam angle was measured. Starting at the nominal input angle, defined as 0 degrees, the input count rate was measured. The detector was then

yawed to +6 and – 6 degrees and translated back to place the beam on the same X location and the count rate was again determined. The results of this test are shown in Figure 11 for Segment A of FUV01. We typically collected ~100,000 counts in each integration, however, the background that was subtracted sometimes varied on the order of 500 cts so we estimate the relative errors on these points of ± 1%. Given this error estimate, the trend in Segment A of lower response at smaller angles of a few percent is real, while Segment B was consistent with no angular variation. Similarly, for FUV02, the variation with angle for Seg. A was a few percent and Seg. B showed no angular variation.

3.6 Pre-conditioning Scrub

The pre-conditioning of the COS FUV01 detector by illuminating it with a high flux of FUV photons at low gain is called a "scrub"[8]. The purpose of the scrub is to reduce the rate of change of the gain loss due to illumination. A scrub does this by removing adsorbed gases from the microchannel walls and accelerating the ion migration in the microchannel surface that tends to lower gain as a function of extracted charge. The scrub continues until the specification on gain sag is met, i.e. the rate of gain loss is less than 100% per Coulomb cm^{-2}.

FUV-01 was installed in a vacuum tank with the input aperture directed towards a sapphire window in the tank. Directly in front of the detector baffle in the vacuum was a sapphire diffuser covering the whole input aperture and approximately 15 cm away from the MCP surface. The diffuser was required to prevent QE and Ion repeller grid shadows which would result in an uneven, structured gain pattern. Outside the vacuum window, a deuterium lamp was placed such that its MgF_2 output window was directly in contact with a CaF_2 diffuser which was a few mm's from the vacuum window. FUV-01 was in its final flight configuration internally and the door could be opened and closed in the vacuum. This door will not be opened in atmosphere again to maintain this scrub condition

After an initial pre-scrub functional, the scrub was started on Feb. 24 and ended on March 8, 2001. Initially the flux was adjusted to give a current of 1 µA per segment at a gain of approximately 75,000. A lower gain level scrub is chosen so that the channel wall conditioning occurs deeper into the microchannels from the rear. As the gain decreased rapidly, the voltage was adjusted periodically to return to the initial current. We started at this current to get through the initial outgassing phase of the scrub where most of the gain decrease is caused by the removal of adsorbed gasses in the plates. After ~40 hours, the scrub was increased to 2µA by increasing the gain of the scrub (~150,000), leaving the illumination constant. This target current was maintained until hour 140 when the target current was raised to 3µA by increasing the illumination flux. This current was

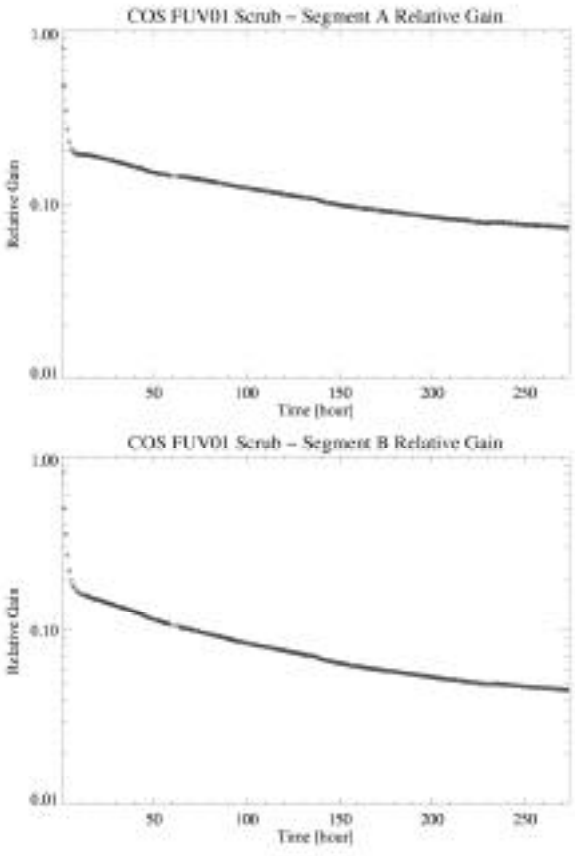

Figure 12. Relative gain vs. time for FUV-01 scrub. Initial quick gain drop is due to the removal of adsorbed gasses while the slower gain sag is the result of a change of the secondary electron emission coefficient of the microchannel walls due to elemental migration

maintained until hour 225 when the flux was attenuated and the gain increased substantially to approximately 20% of the nominal gain of 1pC or 1.25 million where we ran at 2 µA until the end (equivalent to 10 million counts per second). The justification of the high gain scrub at the end was to mimic more flight like gain conditions in an accelerated fashion.

Figure 12 is a plot of the relative gain, where we have normalized the current at every voltage/illumination change to compare to the initial gain. But since we changed the illumination during the course of the scrub, its is just a qualitative indicator of the scrub progress The first 10 hours show the quick rate of gain degradation and the remainder of the graph just the slow approach to the gain plateau. The final decision on when to end the scrub was based on the change of the nominal gain that was determined by the periodic functional tests. Figure 13 shows the gain-voltage plots for both segments taken at various stages of the scrub. The last two functional tests showed less than a 2% gain sag at nominal gain after a differential charge extraction of 0.03 C cm^{-2} (~66%/ C cm^{-2}). The total charge extracted was 0.27 and 0.25 C cm^{-2} for Segments A and B respectively.

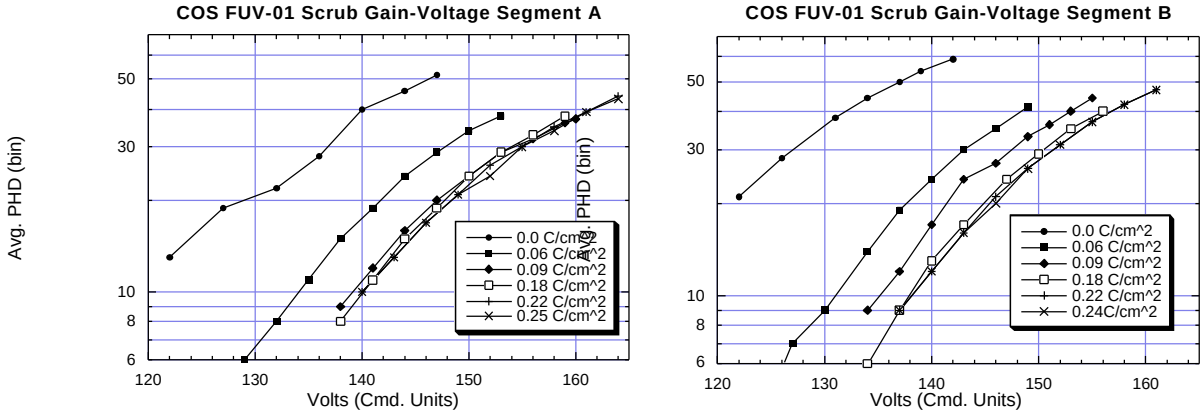

Figure 13. Gain vs. voltage bias during the pre-conditioning scrub of FUV-01. Segment A is the left graph while Segment B is the right. Each curve was aquired after a given integral charge was extracted from the plates. Note how the curves bunch up after this large charge extraction, indicating the gain sag has approached a plateau. An average pulse height (PHD) of bin 40 corresponds to a gain of 1.1pC/event. A high voltage command unit of of 160 corresponds to a voltage of –5010 Volts.

3.7 Deep Flat Field

One of the last tests performed at Berkeley on FUV-01 was to collect a deep flat field at FUV wavelengths. We used the same setup and illumination conditions as the pre-conditioning scrub, but attenuated the flux to approximately 20,000 cps for each segment. The purpose of the test was not to calibrate the relative response per pixel, but rather to estimate what the variations will be in orbit. This was the last time that a relatively uniform illumination of the whole detector field of view would take place. In orbit, there is a light source that will illuminate the detector through the optics at the correct f number and wavelength which will be used to measure the pixel to pixel variation in response. However, the detector will only be illuminated where the source spectra land.

The flat field data were taken in event list mode. Approximately one billion events per segment were collected over a time interval of 50,000 seconds or 13 hours. This is equivalent to ~200 cts per pixel. The HST/COS resolution element for a spectral feature is on the order of 6 x 8 (X,Y) pixels, so this flat field is equivalent to ~10,000 cts per resolution element, or a signal to noise ratio of 100:1. By taking the data in event list mode, we could correct for thermal drifts during this time as well as correct for the geometric distortions discussed in the previous sections.

Figure 14 is a 10 x 9 mm sub-image of the FUV-01 Segment A flat field with the contrast enhanced to show the multifiber boundaries inherent in most high gain MCP imaging detectors. This fixed pattern noise is the result of a small scale imaging distortion caused by a difference in the transverse velocity of the higher gain charge clouds that occur at the multifiber boundaries[9]. Below the image is a plot of 8 rows summed between the two horizontal lines on the image. This plot represents what the fixed pattern noise would look like for a flat continuum spectrum source at high signal to noise, hence the need for flat field data in orbit.

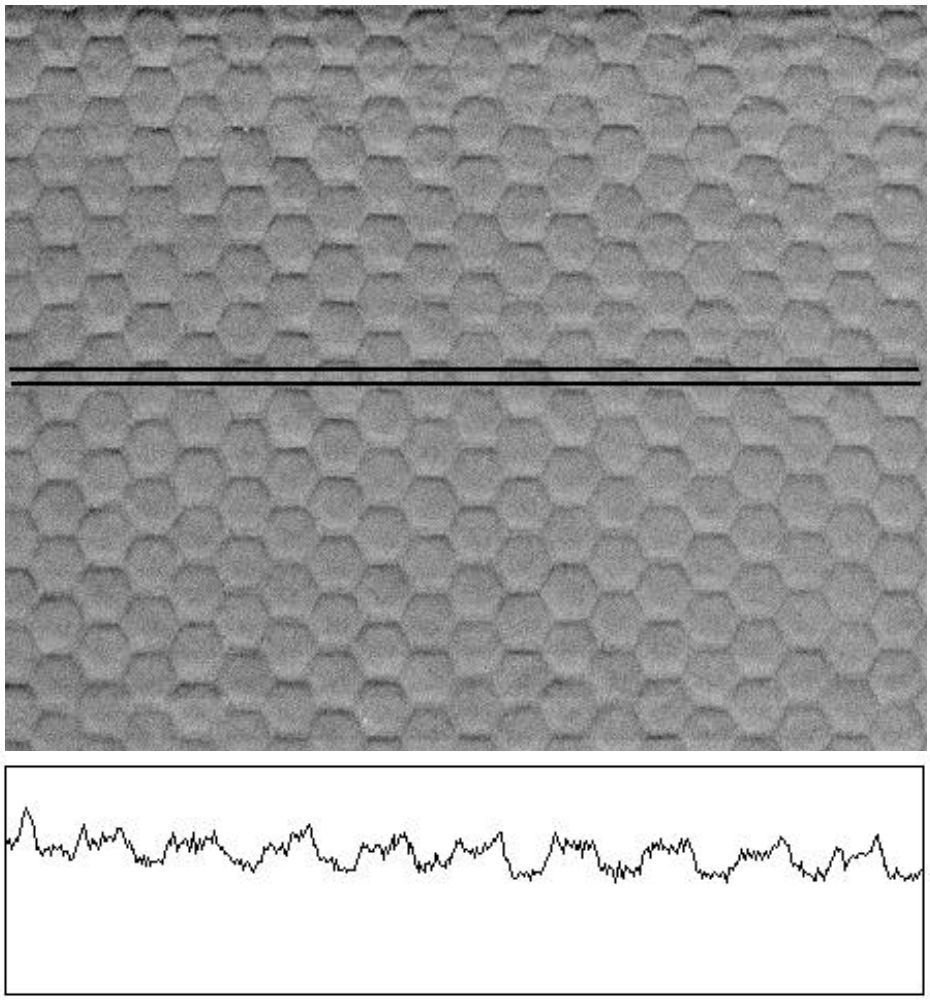

Figure 14. 10 x 9mm image section of a deep flat field (200 cts/pixel) of FUV-01 Segment A. The dominant feature are the hexagonal multifiber boundaries which are an imaging distortion in the Y direction caused by stronger transverse velocities of the higher gain events from these boundaries. The sum of the rows between the two solid horizontal lines is plotted vs. X in the graph below the flat field image to show the contrast of the fixed pattern noise expected for a flat continuum spectrum. The graph bottom represents true zero counts per pixel.

3.8 Gain vs. Voltage and Background Rate

Throughout the testing of the HST/COS detectors, background images and gain-voltage relationship (figure 13) are taken and are part of the standard functional tests performed every time the detector is turned on to high voltage. There is no fixed background image to calibrate as it changes with every

change in environment the detector "sees" and the largest change in the background will come when the detector enters Earth orbit. However, background remains an effective detector health monitor, with sudden changes indicative of possible problems. The FUV-01 background rates when it left Berkeley were ~ 5 and 30 cps for Segments A and B respectively, but they have changed with the coming and going of low gain hotspots (~ 1000 cps) during thermal vacuum testing. If these hotspots reappear in orbit, they can be easily filtered out of the scientific data stream by their low pulse height signature.

ACKNOWLEDGEMENTS

This work was supported by NASA under contract NAS 5-98043

REFERENCES

1. Green, J.C., "Cosmic Origins Spectrograph", *Proc. SPIE*, **4498**, (2000) (this conference)
2. Sahnow, D. et al., "On-Orbit Performance of the Far Ultraviolet Spectroscopic Explorer Satellite", *Ap. J. Lett.*, 538, L7 (2000)
3. Sahnow, D. et al., "On-Orbit Performance of the delay line detectors for the Far Ultraviolet Spectroscopic Explorer", *Proc. SPIE*, **4139**, 149**,** (2000)
4. McPhate, J., Siegmund, O., Gaines, G. Vallerga, J., and Hull, J., "The Cosmic Origins Spectrograph FUV Detector, *Proc. SPIE*, **4139**, 25**,** (2000)
5. Vallerga, J. and McPhate, J., "Optimization of the Readout Electronics for Microchannel Plate Delay Line Anodes", *Proc. SPIE*, **4139**, 34**,** (2000)
6. Wilkinson, E., Penton, S., Beland, S., Vallerga, J., McPahte, J., Sahnow, D., "Algorithms for correcting geometric distortions in delay line anodes", *Proc. SPIE*, **4498**, (2000) (this conference)
7. Lampton, M. and Bixler, J., "Counting efficiency of systems having both paralyzable and nonparalyzable elements", *Review of Scientific Instruments*, 56, 164. (1985)
8. Siegmund, O., "Preconditioning of microchannel plate stacks", *Proc. SPIE* 1072, 111, (1989),
9. Tremsin, A., Vallerga, J., Siegmund, O., "Detector walk in position-sensitive detectors with biased microchannel plates", *Review of Scientific Instruments*, 71, 3758, (2000)